PAPER

Check for updates

Preparation and photocatalytic activity characterization of activated carbon fiber–BiVO$_4$ composites

Chencheng Zhang, [ID] [ab] Pingfang Han, [ID] *[a] Xiaoping Lu,[a] Qinghui Mao,[b] Jiangang Qu[b] and Ya Li[c]

Herein, we describe the hydrothermal immobilization of BiVO$_4$ on activated carbon fibers (ACFs) and characterize the obtained composite by several instrumental techniques, using Reactive Black KN-B (RB5) as a model pollutant for photocatalytic performance evaluation and establishing the experimental conditions yielding maximal photocatalytic activity. The photocatalytic degradation of RB5 is well fitted by a first-order kinetic model, and the good cycling stability and durability of BiVO$_4$@ACFs highlight the potential applicability of the proposed composite. The enhanced photocatalytic activity of BiVO$_4$@ACFs compared to those of BiVO$_4$ and ACFs individually was mechanistically rationalized, and the suggested mechanism was verified by ultraviolet-visible spectroscopy, attenuated total reflectance Fourier-transform infrared spectroscopy, and RB5 degradation experiments. Thus, this work contributes to the development of BiVO$_4$@ACF composites as effective photocatalysts for environmental remediation applications.

Introduction

The development of human society unavoidably causes environmental problems, necessitating the development of highly efficient pollution control methods such as photocatalytic decontamination. In particular, the application of photocatalysis for energy production and environmental protection (*e.g.*, for organic pollutant degradation, hydrogen reduction, and solar cell fabrication) has recently received increased attention.[1–3] In photocatalysts, photoexcited electrons are transferred from the valence band to the conduction band, where they can freely move within the crystal.[4]

TiO$_2$ is a widely used traditional photocatalyst.[5,6] However, its large bandgap (3.2 eV) implies that this catalyst can only utilize ultraviolet light, thus necessitating the development of visible light-driven photocatalysts[7] such as Bi-based semiconductors. For example, BiVO$_4$, first synthesized in 1963, exhibits a relatively narrow bandgap of 2.3–2.4 eV and is therefore a promising photocatalyst.[8] The valence band of BiVO$_4$ mainly comprises the O 2p and V 3d orbitals, which allows photocatalytic O$_2$ evolution under visible light irradiation. The use of BiVO$_4$ to catalyze visible light-induced water splitting was first reported by Kudo *et al.*, who demonstrated a new application of this semiconductor as a photocatalyst[9] and

inspired extensive research on its synthesis, characterization, and photocatalytic properties.[10]

Although photocatalysis has been widely used for the purification of dye-contaminated wastewater with partial contaminant degradation, the separation of spent photocatalysts remains challenging. Separation is typically addressed by immobilizing the active material on macroscopic supports.[11,12] For example, Wu *et al.* reported a novel procedure for immobilizing BiVO$_4$ on silica fibers, obtaining a catalyst with increased surface area and activity.[13] Importantly, the choice of the immobilization method significantly affects the performance of the supported BiVO$_4$, *e.g.*, hydrothermal synthesis commonly yields catalysts with high degrees of crystallinity.

The abundance of delocalized electrons in their conjugated π-systems makes carbon materials promising supports, including fullerenes (C$_{60}$), carbon nanotubes (CNTs), graphitic carbon nitride (g-C$_3$N$_4$), and activated carbon fibers (ACFs), which can potentially enhance charge separation and transport within the immobilized catalyst.[14,15] Among them all, it was observed that the construction of a semiconductor heterojunction can greatly promote photocatalytic activity.[16,17] Recently, ACFs have attracted much attention as pollutant adsorbents because of their high surface areas, diverse functional groups, narrow pore size distributions, and many raw material precursors.[18] However, the adsorption of a given pollutant on ACFs is not accompanied by degradation, and ACFs have therefore been extensively explored as photocatalyst supports offering further photocatalytic performance enhancement. Lin *et al.* described CF-supported ordered mesoporous

[a]Biotechnology and Pharmaceutical Engineering, Nanjing Tech University, Nanjing 210009, PR China. E-mail: hpf@njtech.edu.cn
[b]College of Textile and Garment, Nantong University, Nantong 226019, PR China
[c]Nantong College of Science and Technology, Nantong 226007, PR China

TiO$_2$, revealing that the synergistic active material–support interactions enhanced the photocatalytic activity of this composite to levels exceeding those of commercial photocatalysts.[19] Furthermore, ACF-supported N-doped TiO$_2$ photocatalysts have also been reported.[20] Nevertheless, the immobilization of BiVO$_4$ on ACFs has been underexplored.

Herein, we investigated the hydrothermal immobilization of BiVO$_4$ nanoparticles on ACFs, aiming to (a) develop a simple procedure of immobilizing BiVO$_4$ on ACFs, (b) characterize the structure, properties, and photostability of the synthesized photocatalysts, and (c) determine the influence of the processing parameters on photocatalyst performance.

Experimental

Materials

ACFs were sourced from Nantong Sutong Carbon Fiber Co., Ltd. (Jiangsu, China). Bi(NO$_3$)$_3$·5H$_2$O, NH$_4$VO$_3$, HNO$_3$ (64–69%), NH$_4$OH (35%), KI and ethylenediaminetetraacetic acid (EDTA) of analytical grade were purchased from Meryer Chemical (Shanghai, China). Reactive Black KN-B (RB5) was provided by Bomei Company (Anhui, China). All solutions were prepared using deionized water.

Preparation of photocatalysts

ACFs pretreated with ethanol (95%) and deionized water were dried at 70 °C for 12 h. As shown in Scheme 1, Bi(NO$_3$)$_3$·5H$_2$O (2.1828 g) and a certain amount of EDTA were dissolved in dilute HNO$_3$ (50 mL, 2 mM), and the resulting mixture was stirred at 90 °C for 30 min (200 rpm) with a magnetic stirrer to afford solution A. Solution B was obtained by dissolving NH$_4$VO$_3$ (0.5263 g) in deionized water (50 mL) at 60 °C. Subsequently, a dispersion of ACFs (1.0 g) in solution B was added to solution A, and the pH of the resulting mixture was adjusted by the slow dropwise addition of NH$_4$OH. The above mixture was continuously stirred for 1 h at 50 °C, poured into a Teflon-lined stainless-steel autoclave (150 mL), and maintained at 180 °C for 6 h. The produced precipitate

Scheme 1 Preparation of BiVO$_4$@ACFs.

(BiVO$_4$@ACFs) was washed with ethanol and deionized water several times and dried in a vacuum oven at 75 °C overnight.

Instrumentation

X-ray diffraction (XRD; Ultima IV, Rigaku, Japan) patterns were recorded using high-intensity Cu Kα radiation ($\lambda = 0.154$ nm) in the range of $2\theta = 10$–$80°$ at a scan rate of $5°$ min^{-1}. Sample morphologies and surface elemental compositions were probed by scanning electron microscopy (SEM; JSM6510, JEOL, Japan) coupled with energy-dispersive spectrometry (EDS) at an accelerating voltage of 10 kV, and the sample surface was coated by a thin layer of gold before SEM characterization. The chemical states of the as-prepared composites were determined by X-ray photoelectron spectroscopy (XPS; ESCALAB 250XI, Thermo Electron Corporation, USA). Thermal stabilities were determined by thermogravimetric analysis (TGA; TG209F3, NETZSCH, Germany) performed under N$_2$ in the temperature range of 40–800 °C at a heating rate of 10 °C min^{-1}. Ultraviolet-visible (UV-Vis) absorption spectra were recorded on a UV-Vis spectrophotometer (Cary300, Agilent, USA) in the wavelength range of 200–800 nm. Dye concentrations were monitored by (a) UV-Vis spectroscopy and (b) Fourier-transform infrared (FTIR) spectroscopy (IS10, Thermo Fisher, USA; 600–4000 cm^{-1}) using an attenuated total reflectance (ATR) accessory with a diamond crystal.

Photocatalytic activity evaluation

Photodegradation tests were conducted in a photocatalytic reactor (XPA-XL, XJ, China) equipped with a 1000 W Xe arc lamp as a simulated sunlight source and featuring a 6 cm-diameter water-cooled quartz jacket placed in a stainless steel box. BiVO$_4$@ACFs (0.2 g) and pure ACFs (0.2 g) were independently placed in a quartz tube containing aqueous RB5 (50 mL, 40 mg L^{-1}), and the tube was immediately placed in darkness for 30 min to establish an adsorption equilibrium. Subsequently, the solution was magnetically stirred under visible-light irradiation for 3 h, and the residual dye concentrations were determined spectrophotometrically (V-1200, MAPADA, Shanghai, China). The efficiency of RB5 degradation (R) was calculated as[21]
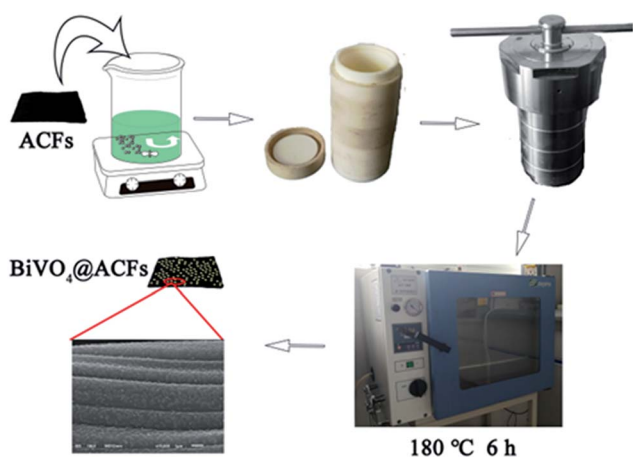
$$R(\%) = (1 - A/A_0) \times 100, \tag{1}$$

where A_0 is the initial absorbance of the RB5 solution and A is the absorbance of the RB5 solution after irradiation.

In addition, to investigate the adsorption kinetics and suggest a possible degradation mechanism, the rate constants of photocatalytic RB5 degradation (k) were obtained from the following equation:[22]

$$\ln(C_0/C) = kt, \tag{2}$$

where C is the concentration of RB5 at time t, C_0 is the adsorption/desorption equilibrium concentration of RB5 at the reaction onset, and C/C_0 is the ratio of the above concentrations determined by absorbance measurements at 598 nm ($C/C_0 = A/A_0$).
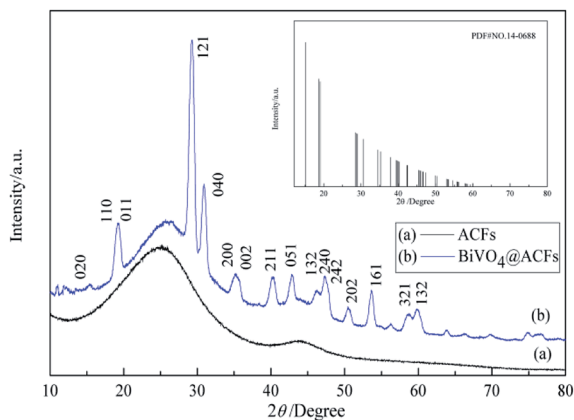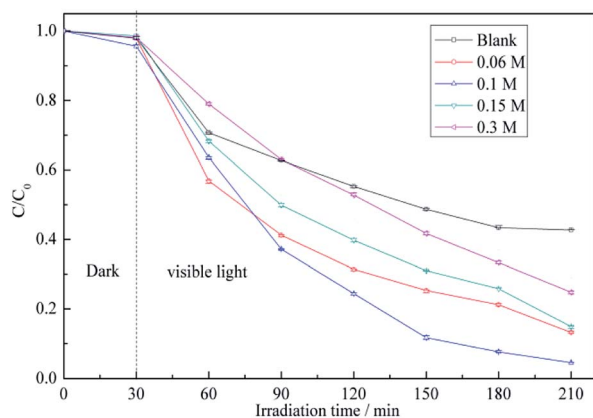
Fig. 4 RB5 degradation profiles determined for different concentrations of precursor solution of $BiVO_4$: (a) pristine ACFs, (b) 0.06 M, (c) 0.1 M, (d) 0.15 M, and (e) 0.3 M.
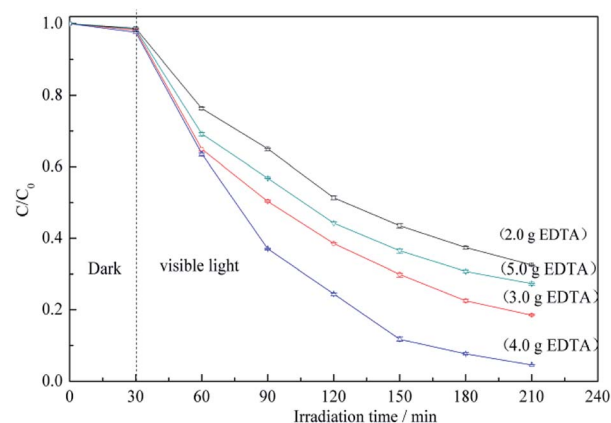

Fig. 6 RB5 degradation profiles determined for different amounts of added EDTA.

synthesis of $BiVO_4$, the addition of EDTA caused the formation of Bi^{3+}–$EDTA^-$ chelates *via* electrostatic interactions.[34] At low Bi^{3+} concentrations, the gradual release of free Bi^{3+} from these complexes induced the formation of small amounts of monoclinic $BiVO_4$.[35] As the concentrations of Bi^{3+} and VO_4^- increased, the inhibitory effect of $EDTA^-$ decreased, which caused the fast growth of particles with large sizes.[36] As the above concentrations continued to increase, the size of the $BiVO_4$ particles became progressively larger, reflecting the decreasing influence of chelation by EDTA, which corresponded to decreased photocatalytic activity.

The above assumption was further supported by TGA results. As shown in Fig. 5, the pristine ACFs exhibit good thermal stability,[37] whereas the thermograms of $BiVO_4$@ACFs recorded at temperatures from ambient to 800 °C show at least two weight losses. The first weight loss (<150 °C, ∼1%) is attributed to the removal of absorbed water,[38] and the second one (150–480 °C, ∼7%) is ascribed to the combustion of EDTA.[39]

Moreover, when the concentration of precursor solution of $BiVO_4$ reaches 0.3 M, $BiVO_4$ loading on the ACFs begins to

decrease. According to the (e)-differential thermogravimetric (DTG) curve in Fig. 5, this is explained by the weak inhibitory effect of high $BiVO_4$ concentration on the growth of $BiVO_4$@-ACFs. Moreover, a further change in $BiVO_4$ crystallites is observed as the temperature reached 700 °C.[40] Therefore, the concentration of precursor solution of $BiVO_4$ in subsequent experiments is set to 0.1 M.

The presence of EDTA, a typical chelator, significantly affects the morphologies and microstructures of $BiVO_4$, because the ligand can be adsorbed on the surface of $BiVO_4$ nanoparticles and can thereby reduce their interfacial energy, with the possible mechanism of the above influence provided below.[41]

$$Bi^{3+} + EDTA^- \rightarrow Bi^{3+}\text{–}EDTA, \tag{3}$$

$$Bi^{3+}\text{–}EDTA + VO_4^- + H_2O \rightarrow BiVO_4 + EDTA^- + 2H^+. \tag{4}$$
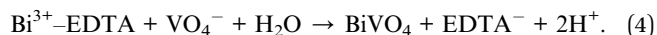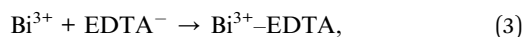
Fig. 6 shows the RB5 degradation profiles recorded in the presence of $BiVO_4$@ACFs samples prepared using different amounts of EDTA. Notably, the fastest photocatalytic degradation is observed for the EDTA loading of 4.0 g. These data indicate that smaller amounts of $BiVO_4$ are coated on ACFs as EDTA decreases, because EDTA balances the growth rates of different crystalline facets.[39] In other words, high EDTA concentrations promote the formation of $BiVO_4$@ACFs samples with irregular rod-like morphologies that show enhanced photodegradation performance.[42] However, when the EDTA loading is further increased to 5.0 g, the photocatalytic activity decreases, because of the negative effects of such high concentrations on the anisotropic growth of single-crystalline $BiVO_4$.[43]

Fig. 7a shows the morphology variation of ACF-supported $BiVO_4$ particles with pH, revealing that higher pH values promotes the lamellar crystallization of $BiVO_4$, which decreases the number of $BiVO_4$ particles.[44] At pH 1, the protonation of EDTA and its precipitation decreases the chelation ability of the ligand, thus allowing the growth of large and highly crystalline $BiVO_4$ particles (Fig. 7a(S1)), which corresponds to low photocatalytic activity.[45] Samples prepared at pH 3 and 5 exhibit

Fig. 5 TGA curves obtained for different concentrations of precursor solution of $BiVO_4$: (a) pristine ACFs, (b) 0.06 M, (c) 0.1 M, (d) 0.15 M, and (e) 0.3 M.

Fig. 7 Morphologies (a) and photocatalytic performances (b) of BiVO$_4$@ACFs prepared at different pH.

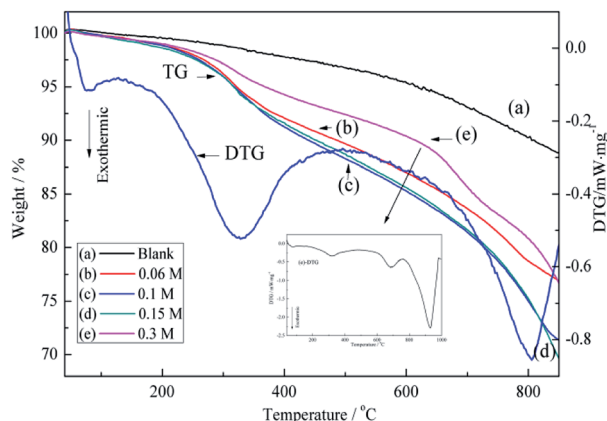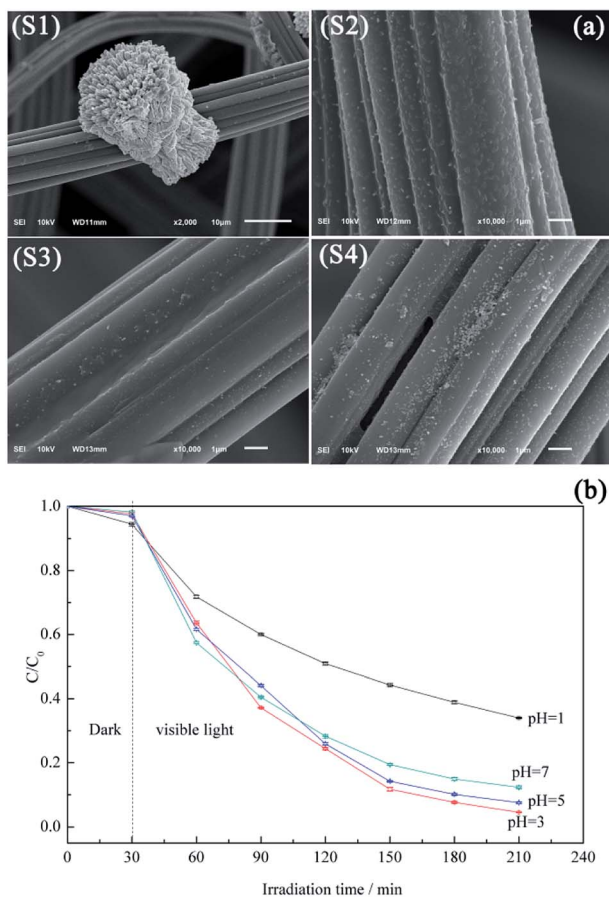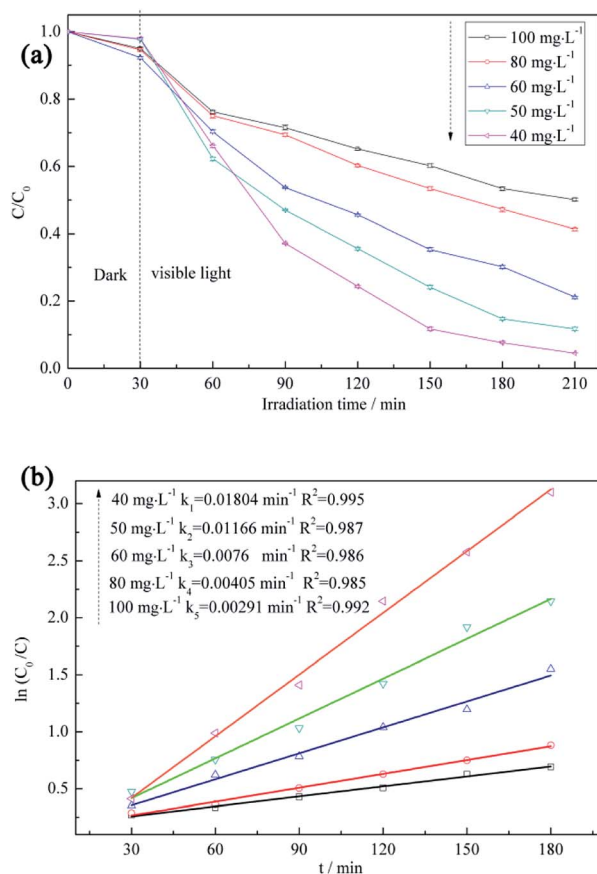Fig. 8 (a) RB5 degradation profiles recorded at different initial RB5 concentrations and (b) first-order kinetics describing the adsorption of RB5 on BiVO$_4$@ACFs.

irregular rod-like morphologies (Fig. 7a(S2 and S3), respectively) and show good photocatalytic activities (Fig. 7b). At these pH values, the increased extent of branching decreases the BiVO$_4$ particle size, which is ascribed to the accelerated hydrolysis of bismuth nitrate and the extensive precipitation of the poorly water-soluble BiONO$_3$.[46] As the pH further increases to 7.0, large numbers of pellet-like particles are produced (Fig. 7a(S4)), attributed to the crystal growth rate exceeding the nucleation rate.[47] However, this observation is also explained by the reduced crystal surface area and the weakened chelation ability of EDTA.[48,49]

Photocatalytic degradation performance of as-synthesized samples and a possible mechanistic explanation

Five initial RB5 concentrations (40, 50, 60, 80, and 100 mg L^{-1}) are used to determine the effect of the above parameter on the degradation rate (Fig. 8a). The photodegradation efficiency is increased with decreasing initial RB5 concentration, which is mainly attributed to the reduction of light penetration efficiency (i.e., the decreased amount of photons arriving at the catalyst surface) at high initial concentrations.[50] Moreover, as the initial RB5 concentration decreases, the slope of the ln(C_0/C) vs. t plot becomes steeper (Fig. 8b), which indicates the existence of a certain linear correlation between these parameters at

different initial RB5 concentrations and implies that the photocatalytic degradation of RB5 is a first-order reaction.[51]

Sample durability was evaluated by using a given specimen for multiple degradation runs. The recycling test was performed three times and all samples were washed with deionized water and ethanol and subsequently dried at 75 °C for 2 h.

Fig. 9a shows that the photocatalytic activity of BiVO$_4$@ACFs remains stable in the first two cycles and exceeds that of pristine ACFs at all times. In the third cycle, 65% of RB5 is removed by 2 h photolysis, which confirms that the BiVO$_4$@ACFs sample is less affected than ACFs during oxidation. On the contrary, the RB5 removal efficiency of only 20% is obtained by ACFs in the third cycle. Therefore, it is concluded that dye molecules and intermediates compete with each other for the limited adsorption and catalytic sites on the catalyst surface, which decreases the photodegradation efficiency.[52] In addition, the morphologies and phases of the used BiVO$_4$@ACFs were further investigated. As shown in Fig. 9b, the used BiVO$_4$@ACFs exhibits almost no difference in SEM images and XRD patterns compared with those obtained before photocatalytic reaction, and the used BiVO$_4$ remains firmly attached to the surface of ACFs, rather than easily exfoliated from the mechanical stirring of the RB5 solutions for long durations. Moreover, the spent catalysts are easily separated from the reaction system.[24]
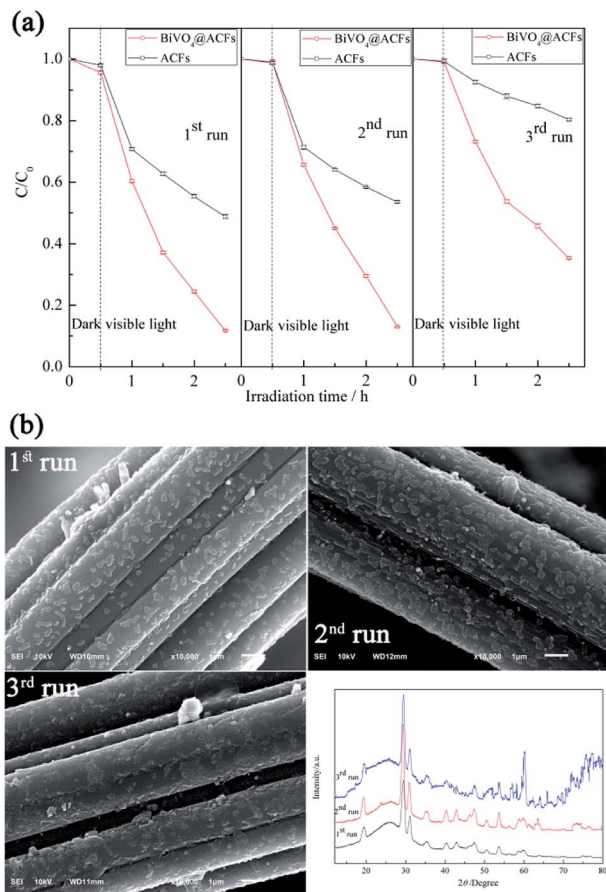
Fig. 9 (a) Performances of tested samples in three consecutive RB5 photodegradation runs; (b) morphologies and XRD patterns of BiVO$_4$@ACFs after RB5 degradation.

Fig. 10a compares the UV-Vis diffuse reflectance spectra of ACFs, BiVO$_4$@ACFs, and BiVO$_4$, revealing that all samples except for BiVO$_4$ exhibit strong absorption in the visible-light region (400–800 nm), as indirectly confirmed by the black hue of the ACFs.[53] These results clearly demonstrate that the intense absorption of visible light by BiVO$_4$@ACFs provide greater photocatalytic activity than shown by pristine ACFs and BiVO$_4$ individually.

The time-dependent UV-Vis spectrum of RB5 (40 mg L^{-1}) recorded under visible light irradiation in the presence of BiVO$_4$@ACFs (0.2 g) (Fig. 10b) reveals the presence of two main absorption peaks. The first peak is located in the visible region (598 nm) and reflects the presence of the azo (–N=N–) chromophore, whereas the second is located in the UV region (310 nm) and reflects the presence of naphthalene rings.[54] Both peaks lose intensity and eventually disappear with increased irradiation time, corresponding to the degradation of RB5.[55]

Structural and elemental analyses of RB5 before and after irradiation were performed using ATR-FTIR spectroscopy. The spectrum of pristine RB5 (Fig. 10c) features a peak at 3436 cm^{-1} assigned to O–H stretching of alcohols and N–H stretching of amines. Peaks at 2927 and 2854 cm^{-1} are assigned to CH$_3$ asymmetric and symmetric vibrations and to CH$_2$ asymmetric vibrational stretching, respectively. The typical peak at 1492 cm^{-1} is assigned to aromatic ring-bonded –N=N– moieties, and that at 1122 cm^{-1} is attributed to sulfoxide (S=O) groups.[56] In contrast, the ATR-FTIR spectrum of RB5 after photocatalytic degradation (Fig. 10c) shows no peak at 1492 cm^{-1}, indicating the breakage of the azo bond, and the appearance of the peak at 1589 cm^{-1} is thought to reflect the formation of quinine-like structures.[57]

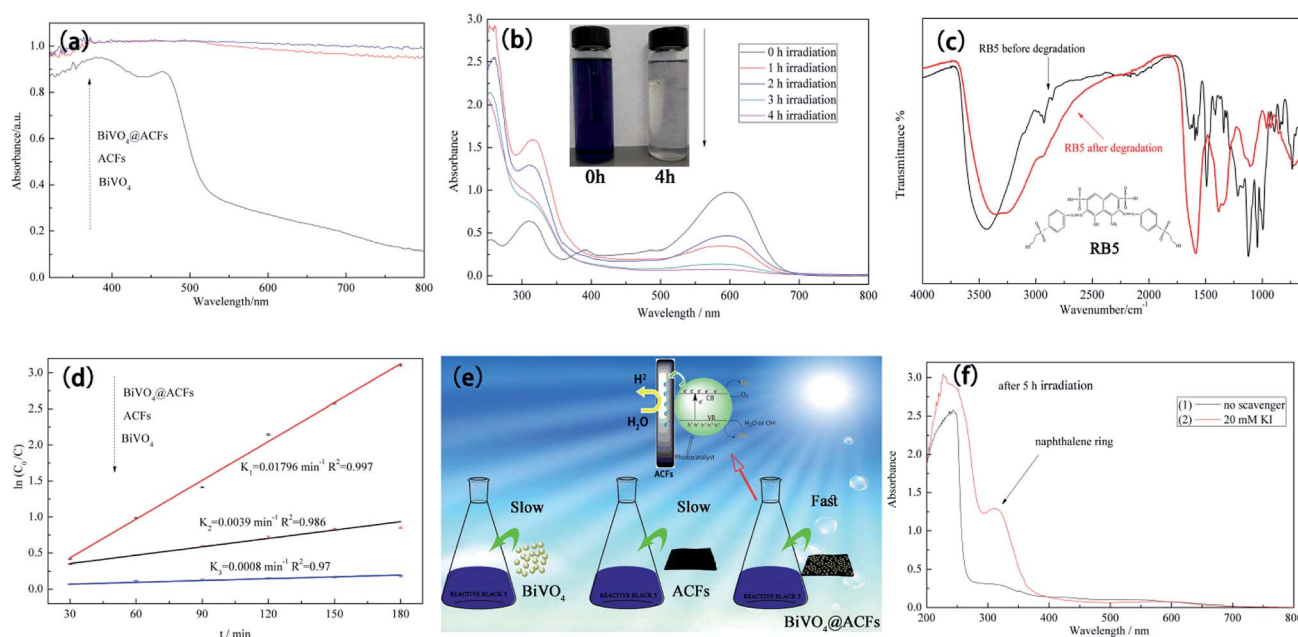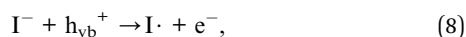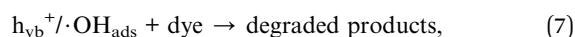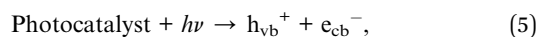
Fig. 10 (a) UV-Vis diffuse reflectance spectra of ACFs, BiVO$_4$@ACFs, and BiVO$_4$; (b) time-dependent UV-Vis spectrum of RB5; (c) ATR-FTIR spectra of pristine and decomposed RB5; (d) RB5 degradation kinetics of different samples; (e) schematic representing the origin of the enhanced photocatalytic activity of BiVO$_4$@ACFs; (f) effects of scavengers on photodegradation of 40 mg L^{-1} RB5.

To determine the extent of C–BiVO$_4$ coupling in the synthesized heterostructures, we explored the photocatalytic activities of ACFs, BiVO$_4$ nanoparticles, and BiVO$_4$@ACFs for the visible light-driven degradation of RB5. Fig. 10d shows the results of kinetic data fitting obtained for the photo-degradation of RB5 solution (40 mg L^{-1}) under visible light illumination, revealing that the k value (0.01796 min^{-1}) of BiVO$_4$@ACFs is much higher than those of ACFs (0.0039 min^{-1}) and BiVO$_4$ (0.0008 min^{-1}).

The formation mechanism of BiVO$_4$@ACFs is represented in Fig. 10e. In the above composite, the highly conductive ACFs act as both charge carriers and electronic transmission media,[58] allowing fast electron transfer from ACFs to BiVO$_4$ and highly efficient dye degradation upon visible-light irradiation.[59] Moreover, water adsorbed on the sample surface reacts with the photogenerated holes (h$_{vb}^+$) to afford ·OH$_{ads}$ radicals as strong oxidizing agents.[60] Hence, the azo bond of RB5 is easily attacked and cleaved by the above radicals, causing dye degradation, as summarized in eqn (5)–(7).[61]

$$\text{Photocatalyst} + h\nu \rightarrow h_{vb}^+ + e_{cb}^-, \tag{5}$$

$$h_{vb}^+ + OH^-_{ads} \rightarrow \cdot OH_{ads}, \tag{6}$$

$$h_{vb}^+/\cdot OH_{ads} + \text{dye} \rightarrow \text{degraded products}, \tag{7}$$

$$I^- + h_{vb}^+ \rightarrow I\cdot + e^-, \tag{8}$$

$$I^- + \cdot OH_{ads} \rightarrow I\cdot + OH^-. \tag{9}$$

The proposed mechanism was further verified by KI, which reacts with h$_{vb}^+$ and ·OH$_{ads}$, as summarized in eqn (8) and (9). As shown in Fig. 10f, when 20 mM KI is used as a diagnostic tool, an adsorption peak appears at 227 nm, and the peak located in the visible region (310 nm) does not disappear. This result displays that the naphthalene rings are mainly cleaved by reaction with h$_{vb}^+$ and ·OH$_{ads}$.

Conclusions

Herein, we established a facile procedure for immobilizing BiVO$_4$ on ACFs and investigated the photocatalytic activities of the obtained composites. To improve the above activities and meet the requirements of practical applications, the effects of parameters such as the concentrations of the precursor solutions of BiVO$_4$ and EDTA and the initial pH on sample structure and morphology were studied in detail. Based on the results of a series of measurements and performance tests, the above parameters were concluded to have important effects on the morphologies of the as-prepared samples.

Moreover, the photocatalytic decolorization of RB5 was shown to be a first-order reaction. Compared to BiVO$_4$ and ACFs, BiVO$_4$@ACFs exhibited improved visible-light adsorption properties as well as increased stability and charge-separation efficiency, thus featuring enhanced RB5 degradation activity. This activity increase was mainly attributed to the formation of a heterojunction electric field between BiVO$_4$ and ACFs, and a possible mechanism was proposed. Thus, we demonstrated that BiVO$_4$@ACFs is a promising carbon-based material for photocatalysis and environmental applications.

Conflicts of interest

There are no conflicts to declare.

Acknowledgements

Notes and references

1 M. M. Khin, A. S. Nair, V. J. Bahu, R. Murugan and S. Ramakrishna, *Energy Environ. Sci.*, 2012, **5**, 8075–8109.
2 S. Natarajan, H. C. Baiaj and R. J. Tayade, *J. Environ. Sci.*, 2018, **3**, 201–202.
3 C. M. Suarez, S. Hernandez and N. Russo, *Appl. Catal., A*, 2015, **504**, 158–170.
4 A. Selloni, *Nat. Mater.*, 2008, **7**, 613–615.
5 A. Fujishima and K. Honda, *Nature*, 1972, **238**, 37–38.
6 D. Yang, H. Liu, Z. Zheng, Y. Yuan, J. C. Zhao, E. R. Waclawik, X. Ke and H. Zhu, *J. Am. Chem. Soc.*, 2009, **131**, 17885–17893.
7 R. A. He, S. W. Cao, P. Zhou and J. Yu, *Chin. J. Catal.*, 2014, **35**, 989–1007.
8 R. Roth and J. Waring, *Am. Mineral.*, 1963, **18**, 1348–1356.
9 A. Kudo, K. Ueda, H. Kato and I. Mikami, *Catal. Lett.*, 1998, **53**, 229–230.
10 K. R. Tolod, S. Hernandez and N. Russo, *Catalysts*, 2017, **7**, 13.
11 J. Z. Su, L. J. Guo, N. Z. Bao and C. A. Grimes, *Nano Lett.*, 2011, **11**, 1928–1933.
12 L. Dong, X. F. Zhang, X. I. Dong, X. X. Zhang, C. Ma, H. C. Ma, M. Xue and F. Shi, *J. Colloid Interface Sci.*, 2013, **393**, 126–129.
13 Q. Wu, P. F. Chen, L. Zhao, J. Wu, X. M. Qi and W. F. Yao, *Catal. Commun.*, 2014, **49**, 29–33.
14 X. Lin, D. Xu, Y. Xi, R. Zhao, L. N. Zhao, M. S. Song, H. J. Zhai, G. B. Che and L. M. Chang, *Colloids Surf., A*, 2017, **513**, 117–124.
15 X. Lin, Y. Xi, R. Zhao, J. Y. Shi and N. Yan, *RSC Adv.*, 2017, **7**, 53847–53854.
16 X. Lin, D. Xu, S. S. Jiang, F. Xie, M. S. Song, H. J. Zhai, L. N. Zhao, G. B. Che and L. M. Chang, *Catal. Commun.*, 2017, **89**, 96–99.
17 X. Lin, D. Xu, R. Zhao, Y. Xi, L. N. Zhao, M. S. Song, H. J. Zhai, G. B. Che and L. M. Chang, *Sep. Purif. Technol.*, 2017, **178**, 163–168.
18 C. L. Mangun, K. R. Benak, J. Economy and K. L. Foster, *Carbon*, 2001, **39**, 1809–1820.
19 X. Lin, M. Li, Y. J. Li and W. Chen, *RSC Adv.*, 2015, **5**, 105227–105238.

20 X. D. Wang, K. Zhang, X. L. Guo, G. D. Shen and J. Y. Xiang, *New J. Chem.*, 2014, **38**, 6139–6146.

21 C. Gu, S. Xiong, Z. X. Zhong, Y. Wang and W. H. Xing, *RSC Adv.*, 2017, **7**, 22234–22242.

22 J. Y. Gao, C. H. Liu, F. Wang, L. J. Jia, K. J. Duan and T. C. Liu, *Nanoscale Res. Lett.*, 2017, **12**, 377.

23 G. Jiang, X. Li, Z. Wei, X. Wang, T. Jiang, X. Du and W. Chen, *Powder Technol.*, 2014, **261**, 170–175.

24 T. Ahmed, H. L. Zhang, H. B. Xu and Y. Zhang, *Colloids Surf., A*, 2017, **531**, 213–220.

25 J. F. Ma, J. H. Chen, B. Wang and S. Cai, *Mater. Res. Bull.*, 2016, **77**, 253–257.

26 Q. Wu, P. F. Chen, L. Zhao, J. Wu, X. M. Qi and W. F. Yao, *Catal. Commun.*, 2014, **49**, 29–33.

27 J. Y. Gao, C. H. Lin, F. Wang, L. J. Jia, K. J. Duan and T. C. Liu, *Nanoscale Res. Lett.*, 2017, **12**, 377.

28 Z. X. Zhao, H. X. Dai, J. G. Deng, Y. X. Liu and C. T. Au, *Chin. J. Catal.*, 2013, **34**, 1617–1626.

29 A. Saha and D. P. Eyman, *Ind. Eng. Chem. Res.*, 2011, **50**, 9027–9033.

30 W. B. Li, Y. P. Zhang, Y. Y. Bu and Z. Y. Chen, *J. Alloys Compd.*, 2016, **680**, 677–684.

31 C. Gu, S. Xiong, Z. X. Zhong, Y. Wang and W. H. Xing, *RSC Adv.*, 2017, **7**, 22234–22242.

32 J. Fang, H. Fan and G. Dong, *Mater. Lett.*, 2014, **120**, 147–150.

33 R. Wang and L. Cao, *J. Alloys Compd.*, 2017, **722**, 445–451.

34 V. Stavila, R. L. Davidovich, A. Gulea and K. H. Whitemire, *Coord. Chem. Rev.*, 2006, **250**, 2780–2810.

35 W. T. Sun, M. Z. Xie, L. Q. Jiang, Y. B. Luan and H. G. Fu, *J. Solid State Chem.*, 2011, **184**, 3050–2054.

36 M. L. Guan, D. K. Ma, S. W. Hu, Y. J. Chen and S. M. Huang, *Inorg. Chem.*, 2011, **50**, 800–805.

37 C. C. Zhang, L. L. Gong, Q. H. Mao, P. F. Han, X. P. Lu and J. G. Qu, *RSC Adv.*, 2018, **8**, 14414–14421.

38 Z. D. Lu, Q. F. Lu, C. Q. Zheng, Z. F. Yao and J. J. Mu, *J. Alloys Compd.*, 2015, **651**, 29–33.

39 L. Y. Zhang, Z. X. Dai, G. H. Zheng, Z. F. Yao and J. J. Mu, *RSC Adv.*, 2018, **8**, 10654–10664.

40 G. C. Du, Z. H. Sun, Y. Xian, H. J. Chen, H. Jing, D. F. Yin and H. J. Tang, *Iron, Steel, Vanadium, Titanium*, 2015, **5**, 34–39.

41 C. Regmi, G. Gyawall, T. H. Kim, B. Joshi, S. K. Ray, Y. H. Jo and S. W. Lee, *J. Nanosci. Nanotechnol.*, 2016, **16**, 11180–11185.

42 S. M. Sun, W. Z. Wang, L. Zhou and H. L. Xu, *Ind. Eng. Chem. Res.*, 2009, **48**, 1735–1739.

43 G. S. Zhao, W. Liu, Y. Hao, Z. Zhang, Q. Li and S. L. Zang, *Dalton Trans.*, 2018, **47**, 1325–1336.

44 S. M. Thalluri, C. O. Suarez, S. Hermandez, S. Bensaid, G. Saiacco and N. Russo, *Chem. Eng. J.*, 2014, **245**, 124–132.

45 L. Zhou, W. Z. Wang, L. S. Zhang, H. L. Xu and W. Zhu, *J. Phys. Chem. C*, 2007, **111**, 13659–13664.

46 S. Tokunaga, H. Kato and A. Kudo, *Chem. Mater.*, 2001, **13**, 4624–4628.

47 G. Q. Tan, L. L. Zhang, H. T. Ren, S. S. Wei, J. Huang and A. Xia, *ACS Appl. Mater. Interfaces*, 2013, **5**, 5186–5193.

48 D. Wang, H. Jiang, X. Zhong, Q. Xu, Y. Ma, G. Li and C. Li, *Chem.–Eur. J.*, 2011, **17**, 1275–1282.

49 Z. F. Zhu, J. Du, J. Q. Li, Y. L. Zhang and D. G. Liu, *Ceram. Int.*, 2012, **38**, 4827–4834.

50 B. Zhou, X. Zhao, H. J. Liu, J. H. Qu and C. P. Huang, *Appl. Catal., B*, 2010, **99**, 214–221.

51 M. S. Lucas, P. B. Tavares, J. A. Peres, J. L. Faria, M. Rocha, C. Peraia and C. Freire, *Catal. Today*, 2013, **209**, 116–121.

52 H. L. Tan, R. Amal and Y. H. Ng, *J. Mater. Chem. A*, 2017, **5**, 16498–46521.

53 J. W. Shi, H. J. Cui, J. W. Chem, M. L. Fu, B. Xu, H. Y. Luo and Z. L. Ye, *J. Colloid Interface Sci.*, 2012, **388**, 201–208.

54 W. F. Khalik, L. N. Ho, S. A. Ong, C. H. Voon, Y. S. Wong, N. Yusoff, S. L. Lee and S. Y. Yusuf, *Chemosphere*, 2017, **184**, 112–119.

55 S. A. Ong, O. M. Min, L. N. Ho, Y. S. Wong and F. M. Ridwan, *J. Water Reuse Desalin.*, 2011, **14**, 202–207.

56 M. Bilal, T. Rasheed, H. M. N. Iqbal, H. B. Hu, W. Wang and X. H. Zhang, *Environ. Manage.*, 2018, **61**, 171–180.

57 M. Gahlout, S. Gupte and A. Gupte, *3 Biotech*, 2013, **3**, 143–152.

58 T. F. Ma, J. Bai and C. P. Li, *Vacuum*, 2017, **145**, 47–54.

59 G. Manna, R. Bose and N. Pradhan, *Angew. Chem., Int. Ed.*, 2014, **53**, 6743–6746.

60 S. K. Kansal, N. Kaur and S. Singh, *Nanoscale Res. Lett.*, 2009, **4**, 709–716.

61 S. Song, L. J. Xu, Z. H. He and J. M. Chen, *Environ. Sci. Technol.*, 2007, **41**, 5846–5853.